

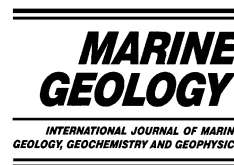


ELSEVIER

Available online at [www.sciencedirect.com](http://www.sciencedirect.com)

SCIENCE @ DIRECT®

Marine Geology 203 (2004) 319–339



[www.elsevier.com/locate/margeo](http://www.elsevier.com/locate/margeo)

# Mechanics of landslide initiation as a shear fracture phenomenon

S.J. Martel\*

*Department of Geology and Geophysics, University of Hawaii, Honolulu, HI 96822, USA*

Accepted 5 September 2003

## Abstract

A 3-D model of shear fracture in an elastic half-space provides insight into the initiation of sliding along weak pre-existing surfaces in rock or consolidated sediments. An elastic model is justified physically if regions of non-elastic deformation associated with sliding are small relative to the size of the shear fracture. A subsurface elliptical shear fracture parallel to the surface simulates sliding at depth along a pre-existing weakness (e.g. a bedding plane). Based on the stress concentration at the shear fracture perimeter, the model predicts landslide scars will tend to have elliptical shapes in map view and width-to-length values of 0.5–1, consistent with many observations. As a shear fracture spreads, the stress concentration at its perimeter promotes its propagation up towards the surface. The model predicts that sliding at depth causes and precedes fracturing at the surface. For a shear fracture less than twice as long as it is wide, surficial fracturing should start in the head and from there ‘unzip’ down along the slide flanks. Depending on the ambient stress state and the shear strength loss at the slide base, a shear fracture might need to become several or more times wider and longer than its depth to develop a sufficiently intense stress concentration to propagate out of plane to the surface. This accounts for the large length-to-thickness ratios of many natural slides. The model also accounts for the following generic landslide characteristics: a steep, arcuate, concave-downhill head scarp; an echelon pattern of opening-mode fractures along the flanks and subparallel to the head scarp trace; subsidence and normal faulting near the head of a slide; and uplift with thrust faulting near the slide toe.

© 2003 Elsevier B.V. All rights reserved.

*Keywords:* landslides; submarine landslides; mechanics; fractures; elasticity

## 1. Introduction

Landslides share many common attributes (Fig. 1). In map view a slide typically is bounded by an arcuate, concave-downhill head scarp, strike-slip faults along its flanks, and a concave uphill toe. The across-slope width of a slide usually is some-

what less than the downslope length, and both are usually much greater than the thickness of a slide. Sliding typically occurs across a surface that is far thinner than the slide mass itself. The failure surface for natural slides commonly coincides, at least in part, with pre-existing geologic structures (e.g. bedding, faults, and joints) but has an overall concave-up, spoon-like shape. Immediately after a slope failure, the failure surface at the head scarp typically is steep or overhanging (i.e. nearly normal to the slope), although a scarp typically de-

\* Tel.: +1-808-9567797; Fax: +1-808-9565154.

E-mail address: [smartel@soest.hawaii.edu](mailto:smartel@soest.hawaii.edu) (S.J. Martel).

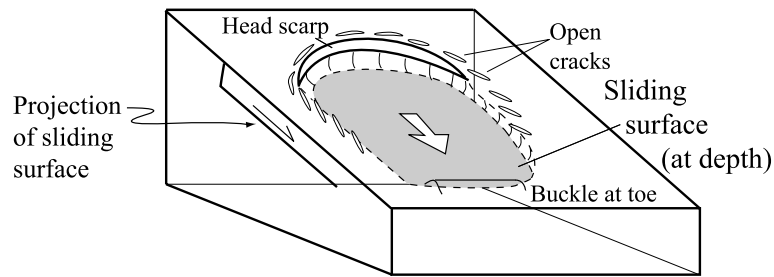


Fig. 1. Characteristics of landslides in an incipient stage of sliding.

grades to a lower angle fairly rapidly. Near the toe the failure surface is at a shallow angle to the slope (Varnes, 1978). Distinctive deformational features form at consistent places within and adjacent to a slide mass. Echelon arrays of fractures, which reflect brittle deformation, commonly open along and subparallel to the head scarp, whereas across-slope buckles commonly develop near the toes. These characteristics occur for slides in a highly diverse range of materials: soils, sediments, rock, snow, and ice. Analyses of sliding should be able to account for how these characteristics develop. Plastic flow models (e.g. Savage and Smith, 1986) account for some of these features in unconsolidated soils, notably the scarp at the landslide head and thrust faults at the toe, but no published physical model accounts for all these features in three dimensions in rock or consolidated sediments. The research here relates these features in a unified physical model. The findings hopefully will be of some practical value in understanding the incipient stages of sliding and mitigating losses caused by slides and tsunamis.

Although the characteristics cited above are best documented for subaerial slides, slides below sea level exhibit similar attributes (Prior et al., 1982; Lee et al., 1991; Schwab et al., 1993; Edwards et al., 1993; Hampton et al., 1995; McAdoo et al., 2000; Tappin et al., 2001) as do those on other planets (e.g. Lucchitta, 1978, 1979). The similar shapes of landslide failure surfaces in markedly different environments allow two key inferences to be drawn about controls on the shape of the failure surface. First, the shape is not strongly controlled by the presence of water, although water pressure changes are key factors in when and where sliding occurs. Second, the

sliding process itself, in conjunction with the distribution of geologic weaknesses in a slope and the type of material, must dictate to a large degree the geometry of a slide mass.

This manuscript presents a simple, quantitative end member model to account for most of these features. It is a 3-D elastic model in which the failure surface at the base of a slide is considered explicitly as a shear fracture. Other end-member models are founded on a plastic flow rheology (e.g. Iverson, 1986; Savage and Smith, 1986; Duncan, 1992). One of the key distinctions between the elastic model presented here and the plastic models is that localized stress concentrations near the perimeter of the region of sliding play a key role here, but not in the plastic models. Another distinction is that in certain plastic models (e.g. Savage and Smith, 1986) much of a slide mass is considered to be in a state of incipient failure; that is not the case here. Predictions of the plastic flow models are consistent with key observations of slides or flows in unconsolidated earth materials, including the prediction of downslope extension and normal faults near the head of a slide, and downslope contraction and thrust faults near the toe. In contrast, an elastic model should be consistent with the incipient stages of sliding, where the strains associated with sliding are small, in consolidated sediments, rock, slab avalanches in snow, and perhaps to some extent in soils strengthened by root mats.

The focus on the sliding process here contrasts with the aim of the limit equilibrium method (LEM), which is widely used to gauge the susceptibility of a slope to sliding. LEM involves calculating the net forces (or moments) that drive sliding, and comparing them to the net forces (or

moments) that might resist sliding along potential slide surfaces in a slope (e.g. [Morgenstern and Price, 1965](#); [Morgenstern and Sangrey, 1978](#)). This manuscript attempts to explain key features and processes outside the realm of LEM. For example:

- How the propagation of a failure surface leads to the slide geometries commonly observed. In LEM, slip is implicitly assumed to initiate simultaneously over the entire surface of failure (which is proscribed in advance), although this is not how natural slides actually develop ([Cruden and Varnes, 1996](#)).

- Deformation in the initial stages of sliding. Standard LEM approaches typically treat earth materials as being rigid and thus cannot account for any deformation, even though deformation typically precedes large displacements of a slide mass and can be very important in monitoring active slides.

- The significance of tensile fracture. Tensile fracture tends to be ignored in LEM, even though it is widely observed in the initial stages of sliding.

This article opens by discussing the how the failure surface of a slide can be treated as a fracture and by outlining some key aspects of fracture mechanics theory. The next section presents how the boundary element method is used to account for gravity-driven slip in a long slope. A description of predicted displacements, propagation tendencies, and stresses associated with a few simple failure surface geometries follows, together with a discussion of the implications for the initial development of landslides. The paper ends by compar-

ing predictions of the elastic model and a plastic flow model with each other and with observations, and by suggesting how the elastic model might be improved.

## 2. The landslide failure surface as a shear fracture

The concentration of relative displacement across a surface that is very thin compared to its in-plane dimensions is characteristic not only of many landslides but also of fractures ([Pollard and Segall, 1987](#)). This motivates an analysis of the landslide failure surface as a fracture (i.e. a surface of finite extent which displacements are discontinuous across). Many people interested in landslides are unfamiliar with fracture mechanics concepts (e.g. [Lawn and Wilshaw, 1975](#)), so a few key concepts are introduced here.

Three modes of fracture describe the relative motion across a fracture near its perimeter: modes I, II, and III. For mode I ([Fig. 2a](#)), the opening mode, the relative displacement  $\Delta u_m = \Delta u_I$  is perpendicular to the fracture plane. Modes II and III pertain to shear motion across a fracture and hence are of particular interest here. Mode II ([Fig. 2b](#)) refers to a relative displacement  $\Delta u_{II}$  parallel to the fracture but perpendicular to the nearby perimeter. Mode III ([Fig. 2c](#)) refers to relative displacement  $\Delta u_{III}$  parallel to both the fracture and the nearby perimeter. A fracture of mode II or mode III can propagate in plane as a shear fracture, but it can also develop mode I secondary fractures near its perimeter that angle

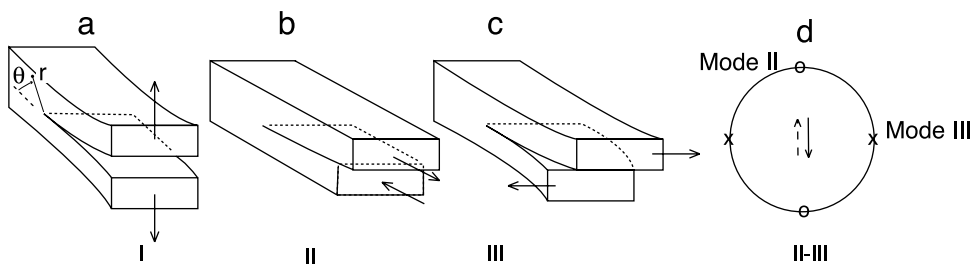


Fig. 2. The three modes of fracturing with the fracture perimeter marked by a dashed horizontal line. (a) Mode I. (b) Mode II. (c) Mode III. (d) Mixed mode II–III fracturing around the circumference of a penny-shaped crack with a constant direction of slip. A cross section downslope through a landslide would show mode II fracturing (sliding) near the head and the toe (circles). A cross section across a landslide would show mode III fracturing (tearing) near the flanks (crosses).

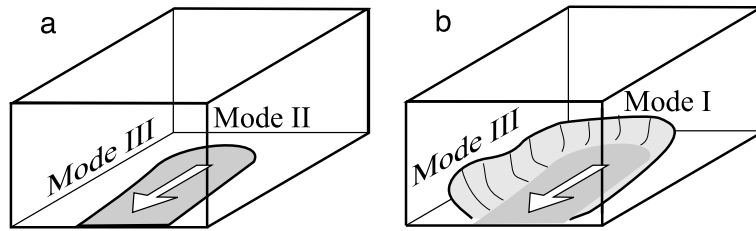


Fig. 3. Conceptual model of rupture surface development proposed by Fleming and Johnson (1989). The arrows point down-slope, in the direction of slip.

or twist out of plane, respectively. A shear fracture with a closed tip line experiences a combination of modes II and III (Figs. 2d and 3).

According to principles of linear elastic fracture mechanics (e.g. Lawn and Wilshaw, 1975), the relative displacement of the fracture walls  $\Delta u_m$  near the perimeter (or tip) of a fracture vary as  $r^{1/2}$ , where  $r$  is the distance from the perimeter, and the stress components  $\sigma_{ij}$  vary as  $r^{-1/2}$ :

$$\Delta u_m = \frac{K_m}{\mu} (r/2\pi)^{1/2} g_m(\nu) \quad (1)$$

$$\sigma_{ij} = K_m (2\pi r)^{-1/2} f_{ij}(\theta) \quad (2)$$

where  $K$  is a constant known as the stress intensity factor,  $\mu$  is the shear modulus,  $g_m$  is a linear function of Poisson's ratio ( $\nu$ ), and  $f$  is a trigonometric function of the angle  $\theta$ , the angle out of the plane of the fracture front (Fig. 2a). Near a fracture tip, where  $r$  is small, strong stress concentrations exist (Eq. 2) even though the relative displacements are small (Eq. 1). The stress concentration intensity is described by  $K$ ; its value depends on the dimensions of the fracture, the stresses driving the relative displacement of the fracture walls, and the geometry of the body containing the fracture. For each of the three modes of fracture, a stress intensity factor exists. The stresses generally vary around the perimeter of a fracture, and so do the stress intensity factors. Stress intensity factors can be used to assess fracture propagation tendencies. A fracture can propagate in plane if the mechanical energy available to propagate the fracture front by an incremental area,  $G$ , is sufficient. The value of  $G$  for in-plane propagation reflects that work that would be done by the near-tip stresses to produce near-tip dis-

placements, and hence  $G$  can be described in terms of  $K$  (Lawn and Wilshaw, 1975):

$$G = G_I + G_{II} + G_{III} = \left( \frac{1-\nu}{2\mu} \right) \left( K_I^2 + K_{II}^2 + \frac{K_{III}^2}{1-\nu} \right) \quad (3)$$

Values of  $G$  at corresponding points on two geometrically identical fractures A and B in identical bodies that are subject to different loading conditions can be compared to assess the relative fracture propagation tendencies (Willemse and Pollard, 2000). Based on Eqs. 1 and 3, the ratio of these  $G$  values, referred to as  $\gamma$ , depends on the ratio of relative displacements at a given small distance  $r$  behind the fracture front:

$$\gamma = \left( \frac{G^A}{G^B} \right) = \frac{(\Delta u_I^2 + \Delta u_{II}^2 + \Delta u_{III}^2 / (1-\nu))^A}{(\Delta u_I^2 + \Delta u_{II}^2 + \Delta u_{III}^2 / (1-\nu))^B} \quad (4)$$

This ratio can be calculated either analytically or numerically. It will be used subsequently to relate  $G^A$  for a shear fracture in a half-space to  $G^B$  for a shear fracture in a full space.

Fracture mechanics principles have illuminated a host of geologic phenomena, including crevasse formation in glaciers (Weertman, 1971), dry slab avalanches (McClung, 1981), and slip surface propagation in soils (Palmer and Rice, 1973), as well as fracture in hard rocks (e.g. Pollard and Aydin, 1988). Palmer and Rice (1973) emphasized that elastic fracture mechanics theory could be applied to the development of a slip surface in over-consolidated clay if non-elastic yielding during sliding is restricted to a small region near the slip surface. They noted that the region of non-elastic yielding could be small relative to the size of a slip surface in a natural slope but still be

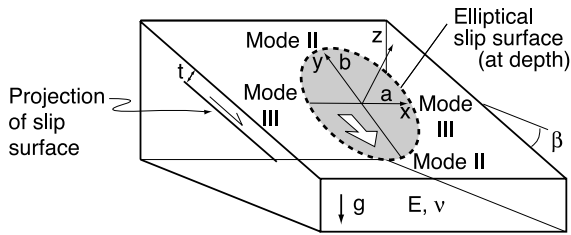


Fig. 4. Coordinate system and idealized elliptical slip patch at base of slide.

large relative to the size of a typical laboratory sample. Palmer and Rice estimated the length of the region of non-elastic deformation near a slide plane tip in an over-consolidated soil as 0.5–2.5 m. This distance is tiny relative to the dimensions of natural slopes. As a result, non-elastic deformation could play a minor role on the scale of many natural slopes, even though it is an integral part of shear failure in laboratory tests on soil samples. Palmer and Rice emphasized the fracture-like attributes of slip surfaces and cautioned against exclusive reliance on laboratory tests of small samples in evaluating how a slip surface develops at the scale of a natural slope.

Fleming and Johnson (1989) proposed a conceptual model that explicitly treats the failure surface of a slide as fracture (Fig. 3). They consid-

ered landslide failure surfaces to nucleate at depth and propagate to the surface, rather than the other way around. McClung (1981) proposed a similar model for the initiation of strain softening in a weak snow layer prior to an avalanche. Fleming and Johnson focused particular attention on the echelon fractures that open along landslide flanks. These fractures compare favorably to those predicted above a vertical mode III fracture in an elastic material (Pollard et al., 1982), where the direction of sliding locally parallels the slide perimeter (Fig. 3). Fleming and Johnson did not, however, employ the model to account for the growth of the failure surface as a whole, for the deformation near the head or toe of a slide mass, or to account for deformation within the body of a slide mass. These points are addressed here.

Encouraged by the work of Fleming and Johnson (1989), Muller and Martel (2000) applied a 2-D mechanical model of shear fracture to investigate the initiation of sliding at depth, subsequent propagation of the failure surface, and the associated surface deformation. They focused on the head and toe of a slide mass in the context of a mode II fracture, where the sliding direction is locally perpendicular to the slide perimeter (Figs. 3 and 4), thus augmenting the work of Fleming and Johnson (1989). Muller and Martel (2000) used a boundary element method (Crouch

Table 1  
Statistics for submarine slumps along the U.S. continental margin (McAdoo, pers. commun., 2003)

Latitude (°)	Longitude (°)	Length (2b) (km)	Width (2a) (km)	Thickness (t) (km)	alb	alt
<i>Oregon</i>						
44.66	−125.42	3	10.7	0.38	3.57	13.1
44.26	−125.44	2.2	1.5	0.34	0.68	2.0
<i>California</i>						
40.01	−124.93	4.3	4.4	0.08	1.02	27.5
39.96	−124.92	2.6	2.4	0.07	0.92	16.8
39.69	−124.47	5.1	6.5	0.23	1.27	13.9
39.25	−124.37	13.1	6.1	0.08	0.47	39.8
<i>Gulf of Mexico</i>						
27.42	−92.49	4.8	13	0.14	2.71	46.4
27.39	−92.37	11.4	6.7	0.15	0.59	22.6
<i>New Jersey</i>						
39.08	−72.6	8.2	6.5	0.13	0.79	25.7
39.02	−72.73	5.1	1.3	0.12	0.25	5.2
38.86	−72.8	5.7	2.5	0.11	0.44	11.2

Slide locations come from McAdoo et al. (2000), as does information to calculate slide thickness.

and Starfield, 1983; Martel and Muller, 2000; Martel, 2000) for a homogeneous, isotropic elastic material in their analyses of slide initiation. Their findings indicate that: (a) slope bases and slope notches promote the nucleation of sliding, which can then propagate upslope, (b) sliding at depth promotes opening of fractures normal to the slope near the head of a slide; and (c) in many cases a shear fracture must grow long relative to its depth to spawn new fractures from its head that propagate to the ground surface unless steep pre-existing geologic weaknesses can be exploited. This last point accounts for the large half-width: thickness ratios commonly observed for landslides (see the  $alt$  ratios in Table 1).

The same approach is extended here to three dimensions. The analysis explicitly accounts for three features required for sliding: (1) a slope, (2) gravitational body forces, and (3) a failure surface. In contrast to the slopes of finite length considered by Muller and Martel (2000), the slopes here are treated as infinitely long. This greatly simplifies the 3-D mathematical treatment and illuminates the mechanics of slides with dimensions that are small relative to slope length. In order to distinguish between the area of slip and the pre-existing weak surface that slip occurs along (e.g. bedding), the area of slip is referred to as a slip patch. The pre-existing weak surface is structurally analogous to a shallow fault parallel

to the surface. Just as an earthquake rupture need not extend over an entire fault, slip need not extend over the entire weak pre-existing surface. To extend the analogy, in both cases slip can nucleate over some small region and then spread.

### 3. Solution method and boundary conditions

The slip patches examined here are elliptical and parallel the surface of a tilted half-space at a distance  $t$  (Fig. 4), so  $t$  equals the thickness of the slide mass. Many slide scars are indeed roughly elliptical in plan view (Cruden and Varnes, 1996), and an elliptical geometry also is common for planar opening mode fractures. The model here simulates sliding along a bedding plane parallel to the surface, a condition common for subaerial slides and perhaps even more common on submarine slopes. The host material is treated as isotropic and uniform, with both the shear modulus ( $\mu$ ) and Poisson's ratio ( $\nu$ ) being constant throughout. The head and the toe of a slide correspond to  $0^\circ$  and  $180^\circ$ , respectively, whereas the centers of the flanks occur at  $\pm 90^\circ$  (Fig. 5). The semi-axis  $a$  is half the across slope width of the slip patch, and the semi-axis  $b$  is half the downslope length (Fig. 4).

In the reference frame used here (Fig. 4), the x-axis points across the slope, the y-axis points

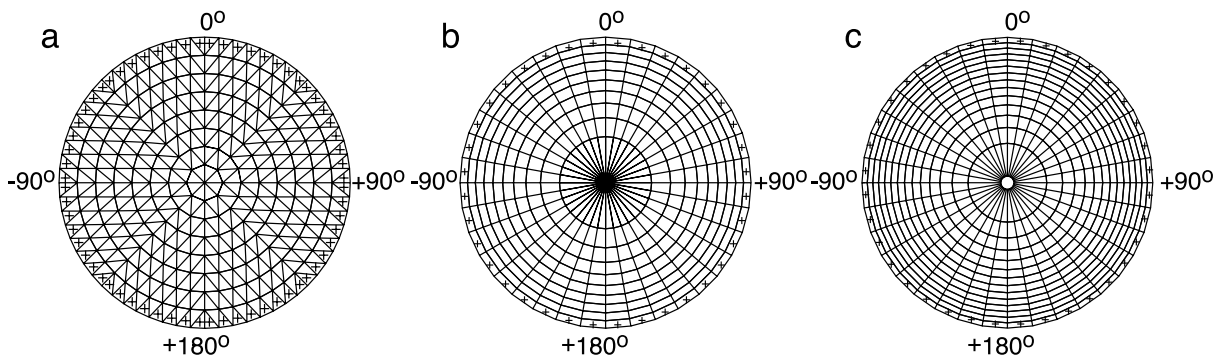


Fig. 5. Element meshes used in the POLY3D calculations. Crosses mark centroids in the outermost elements. (a) A circular slip patch with 512 triangular elements arranged in 8 rings and 8 slices. (b) A circular slip patch with an axisymmetric mesh of 360 triangular and quadrilateral elements. (c) A circular slip patch with an axisymmetric mesh of one 36-sided central polygon and 504 quadrilateral elements. The elements in (b) and (c) are defined such that their vertices would lie on circles (for the central element), sectors (for the triangles) and sections of annuluses (for quadrilaterals) of equal area.

upslope, and the positive z-axis is normal to the slope and points up. The coordinate origin is at a point on the surface of a tilted half-space. Tensile stresses are considered positive, and  $\sigma_1$  refers to the most tensile stress.

The solution for the total stress state around a slip patch ( $\sigma_{ij}^t$ ) can be found by superposing the solutions for: (a) the ambient stress state in the absence of sliding ( $\sigma_{ij}^0$ ), and (b) the stress perturbation due to the slide ( $\Delta\sigma_{ij}$ ), as described by Muller and Martel (2000):

$$\sigma_{ij}^t = \sigma_{ij}^0 + \Delta\sigma_{ij}. \quad (5)$$

The stress perturbation critically affects how slip spreads in an elastic material, yet it is neglected in standard limit equilibrium analyses of slopes and does not enter into plastic flow solutions if the entire slide mass is considered to be on the verge of plastic flow.

A broad range of ambient stress states could be considered. Slope angle, slope height, slope shape, surrounding topography, tectonic forces, elastic material properties, and geologic history all affect the ambient state (Savage, 1994; Savage et al., 1985; Savage and Swolfs, 1986; Martel, 2000; Muller and Martel, 2000). To simplify matters here, the ambient state chosen is for an infinite planar slope of inclination  $\beta$  subject to gravity. The ambient stresses can vary with depth but not with position parallel to the slope surface. The ambient shear stress parallel to the slope is then:

$$\sigma_{zy}^0 = \sigma_{yz}^0 = \rho g z \sin\beta \quad (6)$$

where  $\rho$  is density, and  $g$  is gravitational acceleration. The ambient normal stress perpendicular to the slope is:

$$\sigma_{zz}^0 = \rho g z \cos\beta \quad (7)$$

The ambient slope-parallel normal stresses  $\sigma_{xx}^0$  and  $\sigma_{yy}^0$  are not uniquely defined in an infinite planar slope. Although they do not affect the slip, they are essential components of the total stress state. In the interest of brevity and to keep a sharp focus, the discussion of stresses emphasizes the stress perturbation due to slip, which can be uniquely defined in an infinite planar slope, rather than the total stresses. If the ambient

stresses near the surface are small relative to the stress perturbations, however, then the stress perturbations will reflect the total stresses well (see Eq. 1). Possible effects of slope-parallel normal stresses will be addressed later.

The stress perturbation associated with sliding is found here using the boundary element computer code POLY3D (Thomas, 1993; also see Willemse and Pollard, 2000). This code requires tiling the area of sliding into a mesh of polygonal elements (Fig. 5). The relative motion across a given element is a constant but can differ among elements. POLY3D solves for the relative motion across all the elements necessary to meet the boundary conditions at the element centroids.

The boundary conditions along the elements here are for no relative normal displacement ( $\Delta u_z = 0$ ) and a complete loss of shear strength ( $\sigma'_{zx} = \sigma'_{zy} = 0$ ) across a slip patch. The driving stress  $\Delta\tau$  equals  $-\Delta\sigma_{zy}$ , and for a complete loss of shear strength  $\Delta\tau$  equals  $\rho g z \sin\beta$ . The driving stress will be negative because  $z$  is negative. It can be thought of as driving the upper (positive) side of the slip patch in the downhill (negative  $y$ -) direction. The relative displacement (i.e. slip) across a slip patch scales with the driving stress. A complete loss of shear strength yields the maximum slip and the maximum stress perturbation in the surrounding material, so this scenario provides an end member condition. A complete or nearly complete loss of shear strength could occur in nature by the generation of sufficiently high pore pressures or by the collapse of a flocculated clay structure.

#### 4. Results

The focus here is on slip at depth, slip patch propagation tendencies, and the stress perturbations and displacements at the slope surface above a slip patch. Before considering slip patches in a half-space, a circular slip patch in a full space is examined first. The simple analytical solutions for this full-space problem provide an instructive standard for comparison for half-space problems, for which analytical solutions are not yet available.

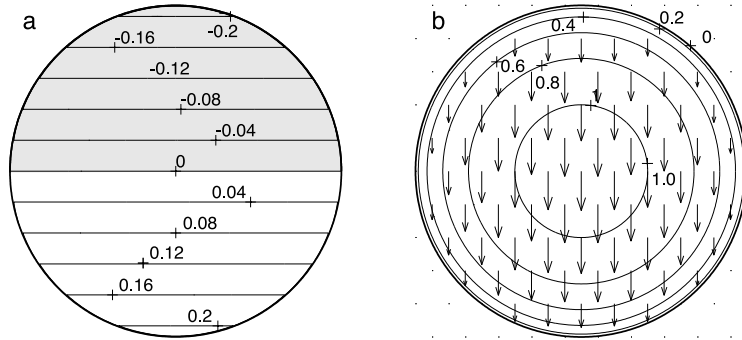


Fig. 6. Analytical solutions from Westman (1965) for displacements and slip along a circular slip patch with a uniform driving stress  $\Delta\tau$  in a full-space. (a) Normalized displacement perpendicular to the slip patch  $(u_z/a)(\mu/\Delta\tau)$ . The displacement is negative (away from the viewer) in the upper half of the figure. (b) Vectors of normalized slip  $(\Delta u/a)(\mu/\Delta\tau)$  superimposed on a contour plot of normalized slip magnitude.

4.1. Circular slip patches in a full-space

This section treats a circular slip patch that experiences a complete loss of shear strength. Four specific points are treated: (1) the ‘absolute’ displacement and relative displacement (i.e. slip) of the opposing walls; (2) the scaling of displacements with slip patch size; (3) the direction of slip; and (4) the distribution of slip across the patch.

The displacements of points on the upper (positive) and lower (negative) walls of a circular slip patch of radius  $a$ , measured relative to a fixed point far from the patch, are obtained from Westman (1965):

$$\frac{u_y}{a} = \pm \left(\frac{4}{\pi}\right) \left(\frac{\Delta\tau}{\mu}\right) \left(\frac{1-\nu}{2-\nu}\right) \sqrt{1-(R/a)^2} \tag{8a}$$

$$\frac{u_x}{a} = 0 \tag{8b}$$

$$\frac{u_z}{a} = \left(\frac{\Delta\tau}{\mu}\right) \left(\frac{1-2\nu}{2-\nu}\right) \left(\frac{y}{2a}\right) \tag{8c}$$

where  $R$  is the distance from the patch center, and  $R \leq a$ . The displacements in the  $y$ - and  $z$ -directions increase linearly with patch radius, and no displacement occurs in the  $x$ -direction. The displacements in the  $y$ -direction of neighboring points on opposing patch walls (Eq. 8a) are equal in magnitude but opposite in sign, with the upper wall being displaced in the negative  $y$ -direction

and the lower wall in the positive  $y$ -direction (recall that  $\Delta\tau$  is negative). Neighboring points on opposing patch walls are displaced equally in the  $z$ -direction in proportion to their  $y$ -coordinates (Eq. 8c), so the patch, together with the surrounding material, rotates uniformly (tilts) about the  $x$ -axis as it slips (Fig. 6a). No displacement of the patch walls relative to one another occurs in the  $z$ -direction: the upper and lower walls rotate equally as the patch slips. Note that both an increase in the shear modulus and an increase in Poisson’s ratio from 0 to 0.5 will diminish the rotation. Interestingly, for a Poisson’s ratio of 0.5, no rotation of a slip patch occurs, but a rotation still does occur along adjacent parallel surfaces (e.g. Pollard and Segall, 1987). Poisson’s ratios near 0.25 are commonly reported for rocks and sediments, so a rotation of the slip patch and surrounding material would be expected for slip in rocks and in consolidated sediments.

The slip  $\Delta u$ , defined here as  $u_{lower} - u_{upper}$  so as to be positive, in this case reflects exclusively the relative displacement in the  $y$ -direction. All the slip vectors parallel the  $y$ -axis (Fig. 6b). Slip peaks at the patch center and drops to zero at the perimeter. Contours of slip are circular. The monotonic increase in slip from the head of the patch ( $0^\circ$ ) to the center reflects a downslope extension of the material there above the slip patch. In contrast, the monotonic decrease in slip from the center of the slip patch to the toe ( $180^\circ$ ) reflects a downslope shortening of the material there

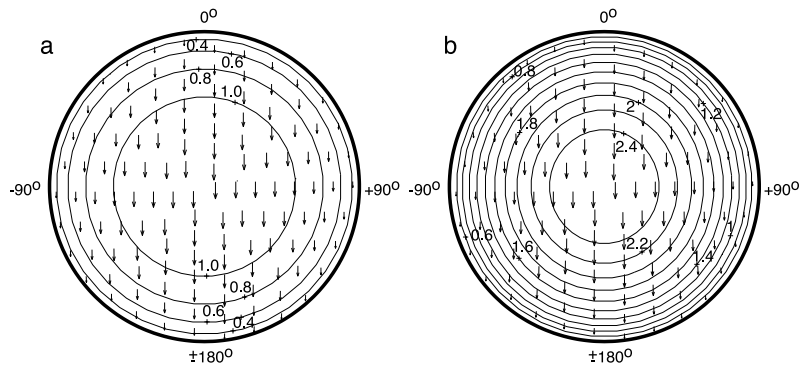


Fig. 7. Vectors and contours of normalized slip  $(\Delta u/a)(\mu/\Delta\tau)$  for circular slip surfaces with different  $a/t$  ratios, calculated using POLY3D. The contour interval is 0.2. (a)  $a/t=1$ . (b)  $a/t=10$ . Here, and in Fig. 8, calculations for the slip vectors use the mesh of Fig. 5a, and calculations for the slip contours use the mesh of Fig. 5b. Contours are not plotted at levels below 0.4. Poisson's ratio = 0.25.

above the slip patch. The slip gradient, and hence the non-zero strains, is largest near the perimeter of the slip patch. The stresses in an elastic material scale with the strains, so the stresses are the largest near the perimeter of the slip patch where the slip vanishes (e.g. Martell, 1997).

#### 4.2. Slip for circular slip patches in a half-space

Tests using slip patches with increasing radius to depth ( $a/t$ ) ratios reveal how slip would vary as a patch grew. The focus remains on circular slip patches rather than a variety of elliptical shapes so that effects of patch size are distinct from those due to patch shape.

Slip in a half-space resembles slip in a full-space in certain ways. Fig. 7 shows slip vectors for  $a/t=1$  and  $a/t=10$ , respectively. The slip is down-dip, peaks at the slip patch center, and drops to zero at the perimeter. Again, this pattern reflects a downslope extension of the upper half of the slide mass and a downslope shortening of lower half.

In other ways, slip in a half-space differs from slip in a full-space. For example, for an isolated circular slip patch growing in a full-space, the maximum slip  $\Delta u_y^*$  scales linearly with the patch radius (Eq. 8a). In contrast, for an isolated circular slip patch growing at a constant depth in a half-space, the maximum slip increases more rapidly than the radius; Fig. 8a shows the case for  $\nu=0.25$ . This difference occurs because as a slip patch grows in a half-space, the slide mass be-

comes relatively thinner (i.e., the  $a/t$  ratio increases) and provides progressively less resistance to sliding. For  $a/t=10$  the maximum slip in a half-space is roughly 2.5 times greater than that for a slip patch of the same radius in a full-space.

The relative values of the maximum displacements of the upper wall ( $u_y^+$ ) and the lower wall ( $u_y^-$ ) of the slip patch also change as a patch grows and the  $a/t$  ratio increases (Fig. 8a). Just as in the full-space case, the upper wall of the patch moves downslope, and the lower wall moves upslope. The upslope displacement of the material immediately below a slide plane might seem non-intuitive, but it is an essential prediction of the elastic model. For  $a \ll t$ , each wall contributes to 50% of the slip (Fig. 8b). As the  $a/t$  ratio increases, the maximum displacement increases on both walls, but on the upper wall it increases more rapidly than the patch radius, whereas on the lower wall it increases about in proportion to the patch radius (Fig. 8a). At  $a/t=10$ , the downslope displacement above the slip patch is about four times greater than the upslope displacement below the slip patch (Fig. 8b). So as a slip patch grows then, not only does the slip increase, but the displacement becomes progressively concentrated above the slide plane, as do the displacement gradients. In contrast, the material below the slip patch behaves as though it were increasingly rigid. This suggests that some of the results here might apply, at least qualitatively, to sliding of a soft material above a more rigid substrate.

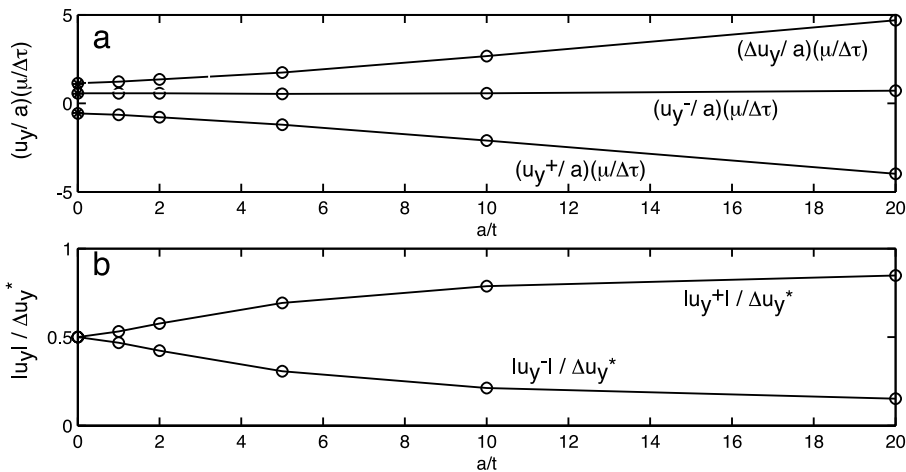


Fig. 8. Numerical solutions for the displacements and relative displacements at the center of a slip patch in a half-space as a function of  $a/t$ . The mesh of Fig. 5c was used for the calculations, and  $\nu=0.25$ . (a) Normalized maximum relative displacement  $(\Delta u_y/a)(\mu/\Delta\tau)$ , normalized maximum displacement of the slip patch upper wall  $(\Delta u_y^+/a)(\mu/\Delta\tau)$ , and normalized maximum displacement of the slip patch lower wall  $(\Delta u_y^-/a)(\mu/\Delta\tau)$ . The ratio  $(\Delta u_y^-/a)(\mu/\Delta\tau)$  is nearly constant. The stars (\*) at the left edge of the plot mark analytic solutions for a slip patch in a full-space. (b) Absolute values of the maximum displacement at the upper ( $u_y^+$ ) and lower ( $u_y^-$ ) sides of a slip patch relative to the maximum slip.

#### 4.3. Slip patch propagation tendencies and slip patch shape

The analyses above indicate how slip will vary as a slip patch grows, assuming it maintains a circular shape. Here the fracture energy release rate  $G$  is used to assess the propagation tendencies of a slip patch and the shape a slip patch might tend to assume as it grows.

The fracture energy release rate  $G$  for an elliptical slip patch in a full space sheds light on the width: length ( $alb$ ) ratio a slip patch might assume when its dimensions are small relative to patch depth (i.e. as  $a/t$  approaches zero). The release of energy during the in-plane propagation of a slip patch, described by Eq. 3, varies around the patch perimeter as a function of the modes II and III contributions. The mechanisms that consume energy during propagation also might vary with fracture mode, but they are not well understood and are not considered here. The focus here is just on the energy release rate  $G$ , along the lines of Willemse and Pollard (2000). The calculations of  $G$  use Eq. 3 and the analytical expressions for the stress intensity factors of Tada et al. (2000). Fig. 9 shows  $G$  as a function of angular position  $\Theta$  around the perimeter of elliptical shear fractures,

with values of  $alb$  ranging from 0.25 to 4, for  $\nu=0$  (Fig. 9a), 0.25 (Fig. 9b), and 0.5 (Fig. 9c). The points on the curves where  $G$  is highest mark places where the greatest amount of energy release occurs and in-plane propagation is the most favorable. In Fig. 9a, for  $alb < 1$  (i.e. a 'relatively long' slip patch), maxima in  $G$  ( $G_{max}$ ) occur at  $\pm 90^\circ$  (the flanks) and minima ( $G_{min}$ ) at  $0^\circ$  and  $\pm 180^\circ$  (the head and toe). A 'relatively long' slip patch thus will preferentially spread from the flanks rather than from the head and toe, causing the  $alb$  ratio to increase towards 1. In contrast, for  $alb > 1$  (i.e. a 'relatively wide' slip patch),  $G_{max}$  occurs at  $0^\circ$  and  $\pm 180^\circ$  (the head and toe) and  $G_{min}$  at  $\pm 90^\circ$  (the flanks). A 'relatively wide' shear fracture thus would spread more readily from the head and toe rather than from the flanks, causing the  $alb$  ratio to decrease towards 1. A slip patch in a full space with a Poisson's ratio of 0 thus would tend to assume a value of  $alb$  of 1 (the flat curve of Fig. 9a) where all points along the slip patch perimeter have an equal tendency to propagate. For a Poisson's ratio of 0.25 and 0.5, slip patches would tend to assume elliptical shapes with  $alb$  values of approximately 0.75 (Fig. 9b) and 0.5 (Fig. 9c), respectively. The results here provide a justification for idealizing a landslide in its initial

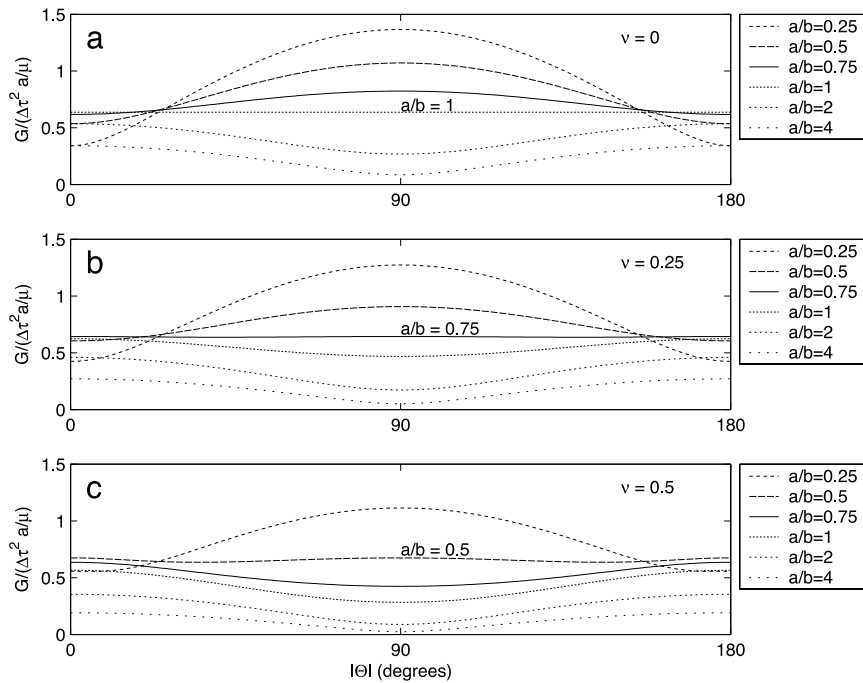


Fig. 9. Values of the normalized fracture energy release rate  $G^*$  ( $G^* = G/(\Delta\tau^2 a/\mu)$ ) as a function of angular position  $\Theta$  around elliptical shear fractures with various ratios of width-to-length ( $a/b$ ) in a full space. The curves are labeled with their  $a/b$  values. (a)  $\nu = 0$ . (b)  $\nu = 0.25$ . (c)  $\nu = 0.5$ . ‘Equilibrium’ ratios are marked by the nearly flat labeled curves.

stages as having an elliptical shape in plane view. Landslides that do not have an elliptical shape might then reflect structural, stratigraphic, topographic, or hydrologic controls not accounted for here.

The behavior of  $G$  for an elliptical slip patch growing in a half space is similar to the full-space behavior but a bit more complicated. The values of  $G$  for a slip patch in a half-space are calculated using the following formula:

$$G = \gamma G^F \tag{9}$$

where  $\gamma$  is the numerically determined ratio of  $G$  for a slip patch in a half-space to  $G$  for a slip patch in a full space (calculated using Eq. 4 and results from POLY3D), and  $G^F$  is the analytical solution for a slip patch in a full-space, calculated using Eq. 3. Fig. 10 shows  $G$  for  $a/b$  ratios of 0.5 (Fig. 10a), 0.75 (Fig. 10b), and 1 (Fig. 10c) as  $alt$  ranges from 0 to 20. Poisson’s ratio equals 0.25 in all these cases. The results indicate that the interaction of a slip patch with the surface becomes progressively pronounced as the slip patch half-

width  $a$  becomes several or more times the slip patch depth  $t$ . Additionally, for  $a/b = 0.5$  (i.e. a ‘relatively long’ slip patch; Fig. 10a)  $G_{max}$  occurs at  $\pm 90^\circ$  (the flanks) and  $G_{min}$  at  $0^\circ$  and  $\pm 180^\circ$  (the head and toe) at all  $alt$  ratios. This behavior also occurs for  $a/b < 0.5$ . So again, a ‘relatively long’ slip patch would spread more readily in plane from the flanks rather than from the head and toe. For  $a/b = 1$  (Fig. 10c),  $G_{max}$  occurs at  $0^\circ$  and  $\pm 180^\circ$  (the head and toe) and  $G_{min}$  at  $\pm 90^\circ$  (the flanks). The magnitude of  $G$  increases with  $alt$ , as does the ratio of  $G_{max}$  to  $G_{min}$ . This behavior is reproduced for  $a/b > 1$ . This means that a ‘relatively wide’ slip patch would spread more readily in plane from the head and toe rather than from the flanks.

For  $a/b = 0.75$  (Fig. 10b), which is the ‘equilibrium value’ for a slip patch in a full space (Fig. 9b), the half-space behavior is a bit more complicated. For  $0 < alt \leq 2$ ,  $G_{min}$  occurs at  $0^\circ$  and  $\pm 180^\circ$  (the head and toe), and  $G_{max}$  occurs at  $\pm 90^\circ$  (the flanks). A relatively small slip patch thus exhibits a weak preferential tendency to wid-

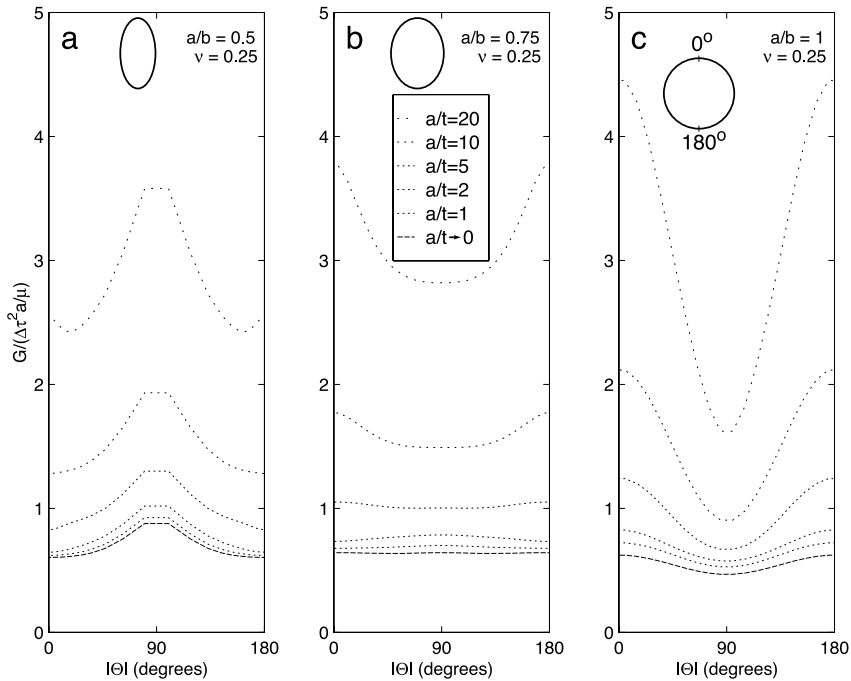


Fig. 10. Values of the normalized fracture energy release rate  $G^*$  ( $G^* = G/(\Delta\tau^2 a/\mu)$ ) where  $\nu = 0.25$  as a function of angular position  $\theta$  around elliptical shear fractures with  $a/b$  ratios of (a) 0.5, (b) 0.75, and (c) 1 as  $a/t$  ranges from 0 to 20.

en and increase its  $a/b$  ratio. For  $a/t \geq 5$ , however,  $G_{max}$  occurs at  $0^\circ$  and  $\pm 180^\circ$  (the head and toe), and  $G_{min}$  occurs at  $\pm 90^\circ$  (the flanks). A relatively large slip patch thus will tend to preferentially lengthen and decrease its  $a/b$  ratio toward 0.5. Based solely on the fracture energy release rate then, a slip patch that spreads in earth materials with a Poisson's ratio of 0.25 would tend to assume an  $a/b$  ratio between 0.75 and 1 when it is small (relative to its depth) and between 0.5 and 0.75 when it is large; landslides would tend to be somewhat longer than they are wide.

Given the variations in conditions and material properties in natural slopes, the results here might be best interpreted as predicting that the distribution of  $a/b$  ratios for a large sample of landslides would peak between 0.5 and 1. This prediction is very much in line with observations. In a study of about 350 landslides in Hokkaido, Japan (Yamagishi and Ito, 1994), nearly all the landslides had a width:length ratio between 0.25 and 4, and for roughly 60% of the landslides the ratio was between 0.4 and 1, consistent with the prediction.

Maps of deep-seated landslides elsewhere (e.g. Voight, 1978) and data from submarine slumps (Table 1) show a similar trend. This suggests that the simple model here is capturing at least some of the essential physics of the sliding process.

The presence of landslides with  $a/b$  ratios less than 0.5 or greater than 1 indicates that factors other than the fracture energy release rate come into play in real slopes. Three particular conditions assumed in the model that might not hold in real slopes could play important roles in determining the width:length ratio of a particular landslide. First, the energy required for across slope propagation (mode III) is assumed to equal the energy required for upslope or downslope propagation (mode II); this might not be true. Second, the weak surface along which sliding occurs is presumed to extend infinitely. In reality, the width and length of a weak surface are finite, and either (or both) could limit the dimensions of a slip patch. Third, the bases of real slides are not perfectly planar; they typically are curved concave

up (at least near the head and toe). This means that real slip patches usually propagate out of plane and so can be influenced by the slope-parallel normal stresses. These points will be discussed further in the remaining sections.

#### 4.4. Displacements and stresses and at the surface for slip patches in a half-space

The discussion now turns to effects that slip at depth would have on the ground surface, where the effects would be most readily observed. Although the fracture energy release rate for a slip patch in a uniform, isotropic material can reveal certain tendencies for how a slip patch might spread, variability in the geologic conditions can be assumed to play a roll as well. For example, if a slip patch grows to the lateral edge of a weak surface, the slip patch might be able to propagate either: (a) in plane only in the upslope direction, or (b) out of plane up to the surface. To account more fully for the possible range of behaviors that might actually occur,  $a/b$  ratios as small as  $1/3$  will be considered here. Additionally, the actual mechanisms of slip patch propagation, which have not been accounted for, might cause the shape of a slip patch to deviate from that predicted on the basis of the in-plane values of  $G$  alone. For example, opening mode fractures characteristically occur near the crown and flanks of slides in many materials, and they could well be an integral part of the propagation of a slip patch to the surface.

As a slip patch grows, the displacements at the ground surface evolve as well. The displacements parallel to the ground surface increasingly resemble those parallel to the slip patch at the slide base, which have already been discussed. The focus here turns to the displacement component perpendicular to the slope surface, which could be monitored with high-resolution bathymetry or altimetry measurements. Fig. 11 shows contours of this component for circular and elliptical slip patches for  $alt$  ratios of 1 and 10 for  $\nu=0.25$ ; qualitatively similar results arise for other values of Poisson's ratio. Five main points emerge. First, subsidence (negative displacement) occurs near the slide head, and uplift (positive displacement)

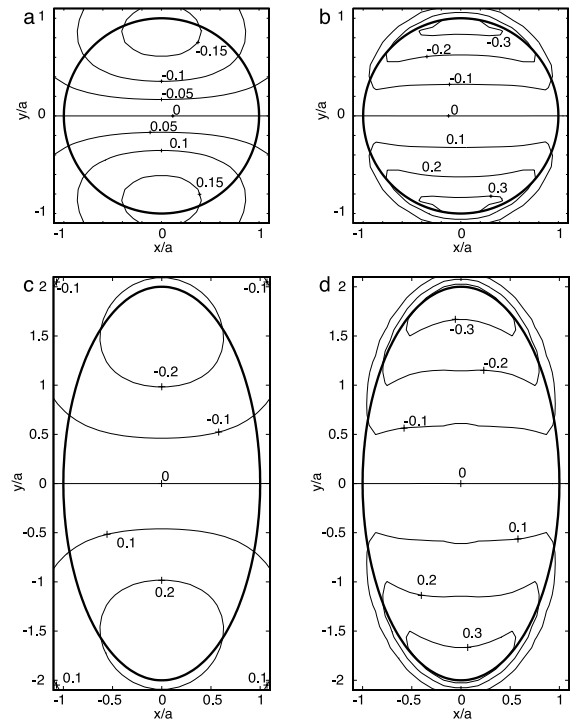


Fig. 11. Normalized displacement perpendicular to the surface  $[(u_z/a)(\mu/\Delta\tau)]$  for circular and elliptical slip patches of various size. (a)  $a/b=1$ ,  $alt=1$ . (b)  $a/b=1$ ,  $alt=10$ . (c)  $a/b=1/2$ ,  $alt=1$ . (d)  $a/b=1/2$ ,  $alt=10$ . Results here, and for Figs. 12–15, are for a model with 900 elements arranged in 15 rings and 60 slices, patterned after Fig. 5b.

occurs at the toe, as is common in real landslides. Second, the ground surface rotates even though the sliding surface is planar: a rotation of the ground surface does not require a curved slide surface. Third, the maximum normalized displacements are about an order of magnitude less than the normalized slope-parallel displacements (Fig. 7). Fourth, the normalized displacement perpendicular to the slope increases with the  $alt$  ratio (e.g. compare the values of the contours in Fig. 11c,d). Fifth, the normalized displacement contours switch from being concave ‘uphill’ near the head of the slide and concave downhill near the toe for  $alt=1$  (Fig. 11a,c), to concave ‘downhill’ near the head of the slide and concave uphill near the toe for  $alt=10$  (Fig. 11b,d). The shapes of the contours for  $alt=10$  are decidedly similar to those typical of real landslides with a large  $alt$  ratio (e.g. Sowers and Royster, 1978). Although

the magnitude of the slope-perpendicular displacements will scale with the driving stress, the shapes of the contours are independent of the driving stress level. As a result, the transition from contours that are concave away from each other to those that are concave towards each other should accompany the growth of slip patches as the half-width of a slide mass becomes several or more times greater than its thickness.

The stresses at the surface also evolve considerably as a slip patch grows. Figs. 12a, 13a, 14a, 15a, and 16a show the magnitude of the normalized perturbation to the most tensile stress ( $\sigma_1$ ) at the surface. Figs. 12b, 13b, 14b, 15b, and 16b show two types of stress trajectories. The light lines (outside the area of the zero contour in Fig. 12a) represent trajectories perpendicular to the most tensile stress where the stress perturbation is positive by light lines. These mark the traces of potential cracks or normal faults. The heavy lines represent trajectories perpendicular to the most compressive stress where the stress perturbation is negative. These mark the traces of potential thrust fault faults or buckles. Whereas these plots deal with perturbations associated with slip, not total stresses, a discussion of the significance of these plots is necessarily somewhat qualitative.

For slip patches where  $a/t=1$  (Figs. 12a and 14a), weak tensile stresses develop in broad re-

gions at the surface above the toe, and weak compressive stresses develop locally near the head. The compressive stresses at the head are much more broadly developed for the circular slip patch of Fig. 12a than the elliptical patch of Fig. 14a. The induced tensile stresses would be unable to open fractures at the surface unless the ambient surface-parallel compressive stresses were very small and the soil had no intrinsic tensile strength. Such conditions might be rare, so surficial cracks are unlikely to open when slip patches nucleate if they are small relative to their depth. If surficial cracks did open, they most likely would be concentrated just above the toe. Cracks would tend to track the trajectories perpendicular to the most tensile stress and hence form a radial pattern at the toe. If opening of radial toe cracks were coupled with closure of cracks (or thrust faulting) at the head, then that would indicate slip patch dimensions that were small relative to patch depth. This would represent behavior at a very early stage of sliding.

As a slip patch propagates, the stress concentrations around its perimeter propagate too, and they intensify. A comparison of slip patches with  $a/t$  ratios of 1 (Figs. 12a and 14a) and 10 (Figs. 13a and 15a) shows that as a patch grows the region of elevated surficial tensile stresses becomes pronounced. The tensile stresses peak slightly downslope of head, are focused above the perim-

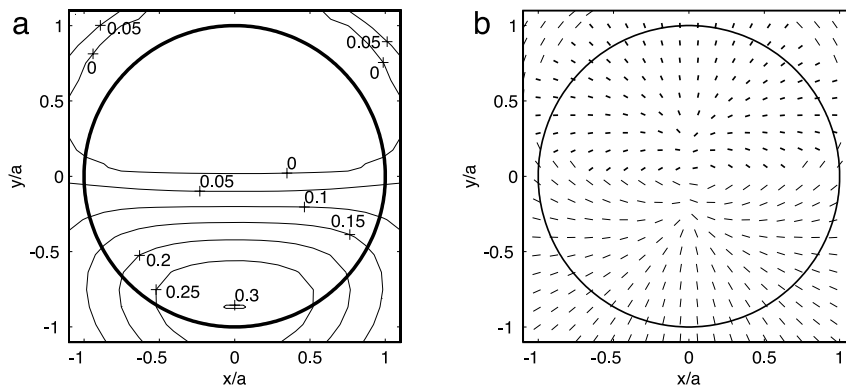


Fig. 12. Magnitudes of (a) the normalized most tensile stress at the surface ( $\sigma_1/(\Delta\tau a/t)$ ) and (b) stress trajectories at the surface for a circular slip patch where  $a/t=1$ . In (b) the light tick marks are perpendicular to the most tensile stress, and the heavy tick marks are perpendicular to the most compressive stress. The light ticks show the potential location and orientation of traces of opening mode fractures and normal faults. The heavy ticks show the potential location and orientation of traces of buckles and thrust faults. This stress trajectory convention also applies to Figs. 13–16.

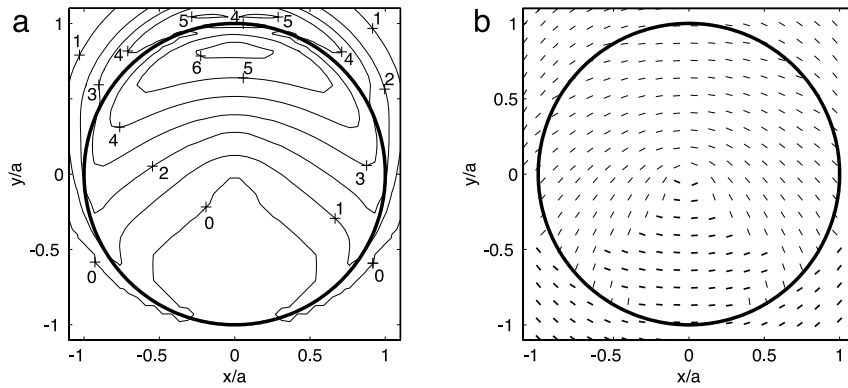


Fig. 13. Magnitudes of (a)  $\sigma_1/(\Delta\tau a/t)$  at the surface and (b) stress trajectories at the surface for a circular slip patch where  $a/t=10$ . Echelon fractures are predicted to open near the head and to parallel the stress trajectories there.

eter of the slip patch, and extend in a crescentic pattern down along the flanks. The normalized peak surficial tensile stresses at the head in Fig. 13a ( $a/t=10$ ) are about twenty times greater than the peak tensile stresses at the toe in Fig. 12a ( $a/t=1$ ). Note that the stress values contoured in these figures, however, are normalized: the values contoured are  $\sigma_1/(\Delta\tau a/t)$ . So as a slip patch grows at a constant depth and its radius increases by a

factor of ten from  $a=t$  to  $a=10t$ , the absolute perturbation in the peak surficial tensile stress increases by a factor of about two hundred, not twenty. The surficial stress perturbation thus increases much more rapidly than the slip patch radius increases as a patch grows.

Figs. 12–15 indicate that if fractures opened up where the tensile stress is sufficiently high, then they should first develop near the head if

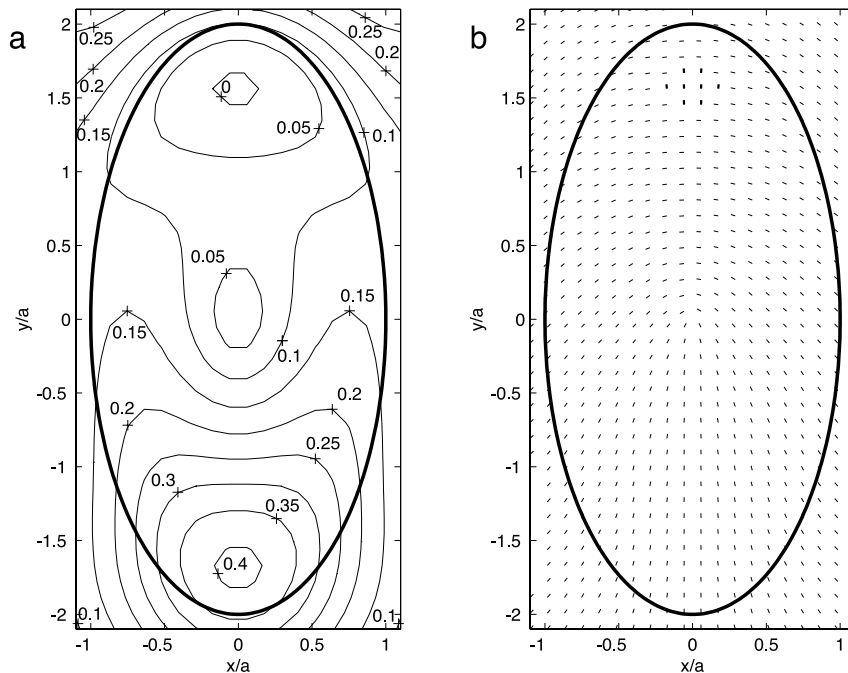


Fig. 14. Magnitudes of (a)  $\sigma_1/(\Delta\tau a/t)$  at the surface and (b) stress trajectories at the surface for an elliptical slip patch ( $a/b=1/2$ ) where  $a/t=1$ .

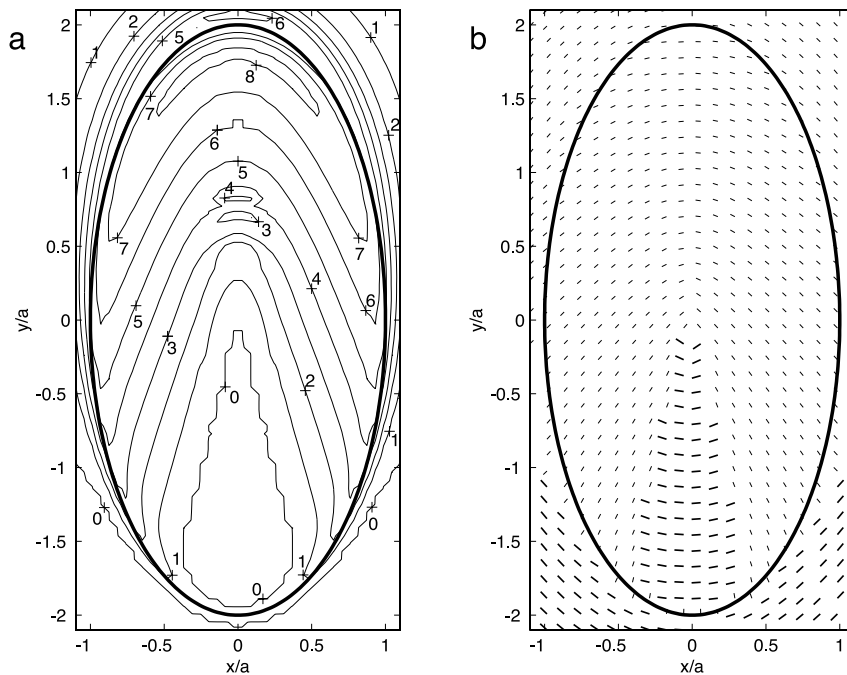


Fig. 15. Magnitudes of (a)  $\sigma_1/(\Delta\tau alt)$  at the surface and (b) stress trajectories at the surface for an elliptical slip patch ( $a/b = 1/2$ ) where  $alt = 10$ . Echelon fractures are predicted to open near the head and to parallel the stress trajectories there.

$a/b > 1/2$ , as is usually the case. The stress concentrations are substantially greater at depth near the slip patch perimeter than at the surface, so cracks at the head also are likely to open at depth and then propagate up to the surface rather than just propagating from the surface down to the slip patch. Opening mode cracks tend to open and grow along principal stress surfaces. As a result, since the topographic surface is free of shear tractions, where surface-parallel tensile stresses exist, opening mode cracks will tend to be perpendicular to the topographic surface, whether it is subaerial, submarine, or on another planet. This will occur no matter whether the opening mode cracks grow up from depth or down from the surface. This would account for why fresh scarps near the head of a landslide commonly are overhanging.

Figs. 13a and 15a suggest that the shape of the eventual scar and the shape of the slip patch before it propagates strongly out of plane should nearly coincide. Note that the peak tensile stresses occur at the slide head ( $0^\circ$ ), not the flanks ( $\pm 90^\circ$ ). From the head, fracturing at the surface would tend to propagate in a zipper-like fashion down

along the flanks. Arcuate zones of echelon fractures that are concave downslope thus indicate a slope that already has progressed substantially to failure, with a significant amount of slip already having occurred at depth. Additionally, the most compressive stress in broad regions near the head has become reoriented in Figs. 13b and 15b such that it is normal to the surface rather than parallel to the surface. This means that fractures there inclined relative to the topographic surface would tend to slip as normal faults; such features are typical at the heads of slides. The most compressive stresses at the toe form a radial pattern. This stress field would promote the formation of buckles and thrust faults at the toe with traces that are concave uphill. The thrust faults would be expected to intersect the surface at an angle of roughly  $30^\circ$ . Such features are common where the toe of a slide mass is displaced well out of a slide scar and can spread (e.g. Cruden and Varnes, 1996) but the results here indicate that they could also form at an incipient stage of sliding.

The scenario for surface fracturing is somewhat different if a slip patch propagates in the direction

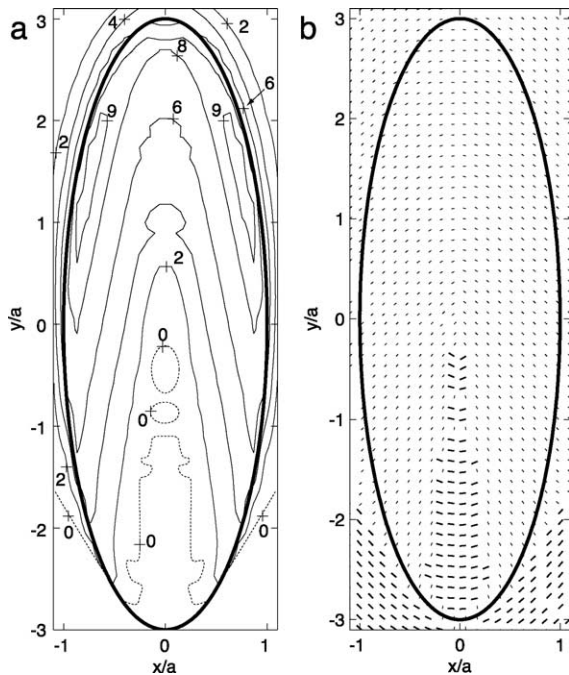


Fig. 16. Magnitudes of (a)  $\sigma_1/(\Delta\tau alt)$  at the surface and (b) stress trajectories at the surface for an elliptical slip patch ( $alb = 1/3$ ) where  $alt = 10$ . Boundary element distribution for model results is analogous to Fig. 5c (505 elements).

of dip but maintains its width. Figs. 13a and 15a indicate the effect of  $b$  doubling while  $a$  remains fixed at  $10t$ . The most tensile stress perturbation at the head of the slide increases by about 1/3, but at the flanks (at  $\pm 90^\circ$ ) it approximately triples. So the tensile stress increases at the ends of the short axis of the slip patch much more rapidly than at the ends of the long axis. The tensile stress still is greatest near the head for  $alb = 1/2$ , but for  $alb \leq 1/3$  the tensile stresses are higher on the flanks (Fig. 16). In that scenario, fracturing at the surface would tend to initiate at the flanks and then propagate towards the head. The site(s) and progression of initial surficial fracturing potentially could be used to determine whether the  $alb$  ratio of a slip patch is greater or less than 1/3.

## 5. Discussion and conclusions

Slip at depth across an elliptical slip patch can

account for some of the most common generic characteristics of landslides:

- Roughly elliptical shapes in map view;
- Large minor axis-to-depth ratios;
- Width-to-length ratios between 0.5 and 1;
- Arcuate, concave downhill head scarps and slope contours;
- Regions of subsidence near the slide head and uplift near the toe;
- Echelon opening mode fractures near the head and flanks;
- Normal faults near the head;
- Thrust faults near the toe.

The elastic model predicts the gross geometry of typical landslides. For the fractures and the faults, the model accounts for their location, orientation, and type. The consistency between a rather broad variety of widely observed features and the model predictions indicates that an elastic model of shear fracture is viable, accounts for some of the key physics, and provides insight into the deformation of slopes in the incipient stages of sliding.

In terms of process, the model predicts that slip at depth over a broad area should precede fracturing at the surface, rather than the other way around. For slip patches that are less than twice as long than they are wide, fracturing at the surface should initiate at the head, then ‘unzip’ down the flanks. Fig. 17 shows a submarine slope off the coast of Santa Barbara, California, that appears to illustrate this process.

The prediction that slip at depth precedes fracturing at the surface has been made previously in the context of fracturing along landslide flanks using both theory and observation. Pollard et al. (1982) showed theoretically how the front of a shear fracture with a mode III component tends to break down into a series of echelon opening mode fractures. Fleming and Johnson (1989) make use of this point and provide corroborating field evidence in their discussion of echelon fractures along the flanks of the Aspen Grove and Twin Lake landslides; they conclude that ‘...strike-slip faults at flanks of the ...landslides propagate from the surface at the base of the landslide toward the ground surface as mode III fractures.... When the strike slip fault reaches the



Fig. 17. Sidescan sonar image of a submarine landslide off the coast of Santa Barbara, California (courtesy of the Monterey Bay Area Aquarium Research Institute). The view is to the east. To the north (left) of the slide the slope appears undeformed. To the south (right) of the slide is a fracture about 4 km long, marked by arrows. This is interpreted to represent fracturing produced in an incipient stage of sliding and to mark the future location of a head scarp.

ground surface it either destroys or integrates the cracks and fault segments that had formed above it.' The analyses here show that an analogous argument applies to the slide head for echelon fracturing at surface in response to mixed mode II–III sliding at depth. Significantly, the echelon fractures clockwise from the apex of the head scarp step to the left, whereas those clockwise from the apex step to the right (Fig. 1). The predicted orientation of cracks along the slide perimeter in Figs. 13b and 15b also show this sense of step. This pattern implies a reversal in the sense of mode III shear (i.e. relative displacement parallel to the slip patch perimeter) along the crown of a slide. An inspection of Figs. 6 and 7 at  $-20^\circ$  and  $+20^\circ$  shows that the model predicts this behavior. This kind of reversal is difficult to explain in the absence of slip at depth. Furthermore, the observed echelon pattern of surficial fractures at the head of a slide appears inconsistent with the fractures growing down from the surface prior to slip. In such a scenario, if the ambient stress field at the surface were uniform, the surficial fractures would tend to form a straight trace perpendicular to the most tensile stress (e.g. Hills et al., 1996; Tada et al., 2000), rather than the observed con-

cave downhill pattern of echelon fractures (Fig. 1). The analyses here thus indicate that slip at depth can cause the observed surficial fracture patterns around the head and flanks of a slide, and that the observed surficial fracture patterns are unlikely to develop without slip at depth.

The prediction that fractures form at the surface at the head of a slide in response to slip at depth, rather than preceding slip at depth, has an important practical implication. It implies that surficial fracturing marks a relatively late stage in landslide initiation, rather than an early stage. Surficial fractures provide a warning that a complete slope failure could be imminent.

An elastic analysis raises the distinct possibility that opening mode fractures propagate away from a slip patch at depth and towards the surface at the head of a slide, in addition to just propagating from the surface down. Even though slip at depth produces a strong finite tensile stress concentration at the surface, elasticity theory predicts a vastly greater (singular) tensile stress concentration at the slip patch tip at depth. To my knowledge, no one has yet described the propagation of opening mode fractures towards the surface at the head of a landslide, but this could be because: (a)

the observations would be hard to make, and (b) no one has considered making the observations. The opening of surficial cracks above a dike propagating towards the surface (e.g. Pollard et al., 1983) shows that upward and downward fracture propagation can occur contemporaneously. In that case, the opening of a dike at depth clearly causes the surficial fractures to open, rather than the converse. Opening mode fractures also are widely documented near the ends of faults exhumed from depths of several kilometers (e.g. Segall and Pollard, 1983; Granier, 1985; Martell, 1997), where confining pressures are vastly larger than those in landslides; this strongly indicates that fractures also could open at depth and propagate up from a landslide slip surface.

A central postulate here is that the stress concentration at the perimeter of a slip patch not only permits it to propagate in plane as a shear fracture but also allows it to propagate out of plane up towards the surface. The extent to which a slip patch propagates in plane before propagating out of plane towards the surface likely depends on the ambient normal stresses parallel to the slope, the materials in a slope, and on variations in stratigraphy, topography, lithification, weathering, and fracture distribution. The range of conditions in nature probably permits a broad range in thickness:width ratios for landslides. A systematic analysis of these factors is beyond the scope of this report, but a few general comments can be made about the probable effect of the ambient normal stresses parallel to a slope. First, the greater the compressive stress parallel to the ground surface (or seafloor) is, the more the opening of fractures normal to the surface would be retarded. The opening of steep fractures at the eventual perimeter of a slide *before* a slope completely fails demonstrates that fracture opening plays an integral role in the development of a landslide and presumably in the propagation of a slip patch up to the ground surface. It follows that the propagation of a failure surface up to the ground surface (or seafloor) also would be retarded by large compressive stresses parallel to the ground surface. Second, if the ambient compressive stresses parallel to the slope are large, then a slip patch will need to spread out over a

large area to generate tensile stress perturbations sufficient to overcome the ambient compressive stresses and allow tensile fracture and out-of-plane propagation of a slip patch to the ground surface. A slip patch would be more likely to propagate parallel to the ground surface at the head or toe, and to turn up at the flanks, if the ambient downslope compressive stresses are larger than the across-slope compressive stresses. Conversely, a slip patch would be more likely to propagate parallel to the surface laterally, and turn up at the head, if the ambient across-slope compressive stresses are larger than the downslope compressive stresses. Measurements of the ambient slope-parallel stresses thus could prove useful in understanding the development of a slide, as would information on the shear strength drop at the base of a slide. Acquiring that information, however, might require a concerted effort.

Predictions of the elastic shear fracture model and the analytical 2-D plastic flow model of Savage and Smith (1986) are similar in some ways but differ in others. Both models consider sliding to originate at depth and propagate to the surface. Both predict downslope extension in the head region of a slide mass and downslope contraction in the toe region. A key difference is that the elastic shear fracture model admits strong stress concentrations, whereas the plastic flow model does not. Among other things, accounting for the stress concentrations allows the elastic model to account for: (a) the relative values of the length, width, and thickness of slide scars, (b) scars with elliptical shapes in plan view, and (c) the commonly observed distribution of opening mode fractures at the surface. On the other hand, the elastic model presented here does not account for pore pressure, but the plastic flow model does, and pore pressure is known to be an important factor in landslides. Poro-elastic solutions exist for displacement discontinuities in two dimensions, however, and could be incorporated into an elastic model (see Wang, 2000). The formation of thrust faults at the slide toe and their propagation up to the ground surface might involve a considerable amount of non-elastic deformation unless pre-existing weaknesses can be exploited, and the plastic flow model might predict thrust fault geometry at

the toe of a slide decidedly better than an elastic model would. An elastic model could also be improved in this regard by accounting for a zone of non-elastic deformation near the fracture perimeter (e.g. Martel and Boger, 1998).

Both stress heterogeneities and stress concentrations are a natural consequence of slip in a deformable medium. They have been cited as key factors in slope stability (Terzaghi, 1950; Peck and Wilson, 1968), yet stress heterogeneities and stress concentrations of the sort described here are not included in standard slope stability analyses. Failure to account for stress heterogeneities and stress concentrations, which could be transient, could lead to over-estimates of slope stability and misinterpretation of evidence bearing on impending slope failure.

### Acknowledgements

Support by the Office of Naval Research through Grant No. N00014-96-1-0353, the U.S. Department of Energy through Grant No. FG03-95ER14525 Amdt #A004, and the National Science Foundation, Division of Ocean Sciences, through Grant No. OCE97-30673, is gratefully acknowledged, as is the support from the National Science Foundation to attend the stimulating workshop on tsunamis and submarine landslides in 2000. I thank William Savage, Phil Watts, and two anonymous reviewers for their constructive criticisms of various drafts of the manuscript. Colleagues at SOEST, notably Ben Brooks, Neil Frazer, Gerard Fryer, Garrett Ito, and Paul Wesel, provided valuable comments at many stages of this study. Josh Roering observed that the results might apply to soil masses strengthened by root mats. Brian McAdoo kindly provided unpublished data on the landslide length and width used in Table 1. This is SOEST contribution 5203.

### References

Crouch, S.L., Starfield, A.M., 1983. Boundary Element Methods in Solid Mechanics. Allen and Unwin, London.  
 Cruden, D.M., Varnes, D.J., 1996. Landslide types and pro-

cesses. In: Turner, A.K., Schuster, R.L. (Eds.), Landslides: Investigation and Mitigation. National Academy of Sciences, Washington, DC, pp. 36–75.  
 Duncan, J.M., 1992. State-of-the-art: Static stability and deformation analysis. In: Seed, R.B., Boulanger, R.W. (Eds.), Stability and Performances of Slopes and Embankments – II. American Society of Civil Engineers, New York, pp. 222–266.  
 Edwards, B.D., Lee, H.J., Field, M.E., 1993. Seismically induced mudflow in Santa Barbara Basin. In: Schwab, W.C., Lee, H.J., Twichell, D.C. (Eds.), Submarine Landslides: Selected Studies in the U.S. Exclusive Economic Zone. U.S. Geol. Surv. Bull. 2002, pp. 167–175.  
 Fleming, R.W., Johnson, A.M., 1989. Structures associated with strike-slip faults that bound landslide elements. Eng. Geol. 27, 39–114.  
 Granier, T., 1985. Origin, damping, and pattern of development of faults in granite. Tectonics 4, 721–737.  
 Hampton, M.A., Lee, H.J., Locat, J., 1995. Submarine landslides. Rev. Geophys. 34, 33–59.  
 Hills, D.A., Kelly, P.A., Dai, D.N., Korunshy, A.M., 1996. Solution of Crack Problems. Kluwer, Dordrecht.  
 Iverson, R.A., 1986. Unsteady, nonuniform landslide motion; 1, Theoretical dynamics and the steady datum state. J. Geol. 94, 1–15.  
 Lawn, B.R., Wilshaw, T.R., 1975. Fracture of Brittle Solids. Cambridge University Press, New York.  
 Lee, H.J., Schwab, W.C., Edwards, B.D., Kayen, R.E., 1991. Quantitative controls on submarine slope failure morphology. Mar. Geotechnol. 10, 143–157.  
 Lucchitta, B.K., 1978. A large landslide on Mars. Geol. Soc. Am. Bull. 89, 1601–1609.  
 Lucchitta, B.K., 1979. Landslides in Valles Marineris. Mars. J. Geophys. Res. 84, 8097–8113.  
 Martel, S.J., 1997. Effects of cohesive zones on small faults and implications for secondary fracturing and fault trace geometry. J. Struct. Geol. 19, 835–847.  
 Martel, S.J., 2000. Modeling elastic stresses in long ridges with the displacement discontinuity method. Pure Appl. Geophys. 157, 1039–1057.  
 Martel, S.J., Boger, W., 1998. Geometry and mechanics of secondary fracturing around small three-dimensional faults in granitic rock. J. Geophys. Res. 103, 21,299–21,314.  
 Martel, S.J., Muller, J., 2000. A two-dimensional boundary element method for calculating elastic gravitational stresses in slopes. Pure Appl. Geophys. 157, 989–1007.  
 McAdoo, B.G., Pratson, L.F., Orange, D.L., 2000. Submarine landslide geomorphology, US continental slope. Mar. Geol. 169, 103–136.  
 McClung, D.M., 1981. Fracture mechanical models of dry slab avalanche release. J. Geophys. Res. 86, 10783–10790.  
 Morgenstern, N.R., Price, V.E., 1965. The analysis of the stability of slip surfaces. Geotechnique 15, 79–93.  
 Morgenstern, N.R., Sangrey, D.A., 1978. Methods of stability analyses. In: Schuster, R.L., Krizek, R.J. (Eds.), Landslides: Analysis and Control. National Academy of Sciences, Washington, DC, pp. 155–171.

- Muller, J., Martell, S.J., 2000. Numerical models of translational landslide rupture surface growth. *Pure Appl. Geophys.* 157, 1009–1038.
- Palmer, A.C., Rice, J.R., 1973. The growth of slip surfaces in the progressive failure of over-consolidated clay. *Philos. Trans. R. Soc. A* 332, 527–548.
- Peck, R., Wilson, S.D., 1968. *The Hind Iuka Landslide and Similar Movements*, Honolulu, Hawaii. Hamilton Library, University of Hawaii, 19 pp.
- Pollard, D.D., Segall, P., 1987. Theoretical displacements and stresses near fractures in rock. In: Atkinson, B.K. (Ed.), *Fracture Mechanics of Rock*. Academic Press, London, pp. 277–348.
- Pollard, D.D., Aydin, A., 1988. Progress in understanding jointing over the past century. *Geol. Soc. Am. Bull.* 100, 1181–1204.
- Pollard, D.D., Segall, P., Delaney, P.T., 1983. Formation and interpretation of dilatant echelon cracks. *Geol. Soc. Am. Bull.* 93, 1291–1303.
- Pollard, D.D., Segall, P., Delaney, P.T., 1982. Formation and interpretation of dilatant echelon cracks. *Geol. Soc. Am. Bull.* 93, 1291–1303.
- Prior, D.B., Bornhold, B.D., Johns, M.W., 1982. Morphology of a submarine slide, Kitimat Arm, British Columbia. *Geology* 10, 588–592.
- Savage, W.Z., 1994. Gravity-induced stresses in finite slopes. *Int. J. Rock Mech. Min. Sci. Geomech. Abstr.* 31, 471–483.
- Savage, W.Z., Swolfs, H.S., 1986. Tectonic and gravitational stress in long symmetric ridges and Valleys. *J. Geophys. Res.* 91, 3677–3685.
- Savage, W.Z., Smith, H.S., 1986. A Model for the Plastic Flow of Landslides. *U.S. Geol. Surv. Bull.* 1385.
- Savage, W.Z., Swolfs, H.S., Powers, P.S., 1985. Gravitational stresses in long symmetric ridges and valleys. *Int. J. Rock Mech. Min. Sci. Geomech. Abstr.* 22, 291–302.
- Schwab, W.C., Lee, H.J., Twichell, D.C. (Eds.), 1993. *Submarine Landslides: Selected Studies in the U.S. Exclusive Economic Zone*. U.S. Geol. Surv. Bull. 2002.
- Segall, P., Pollard, D.D., 1983. Nucleation and growth of strike slip faults in granite. *J. Geophys. Res.* 88, 555–568.
- Sowers, G.F., Royster, D.L., 1978. Field investigation. In: Schuster, R.L., Krizek, R.J. (Eds.), *Landslides: Analysis and Control*. National Academy of Sciences, Washington, DC, pp. 81–111.
- Tada, H., Paris, P., Irwin, G., 2000. *The Stress Analysis of Cracks Handbook*. American Society of Mechanical Engineers, New York.
- Tappin, D.R., Watts, P., McMurtry, G.M., Lafoy, Y., Matsu-moto, T., 2001. The Sissano, Papua New Guinea tsunami of July 1998 – offshore evidence on the source mechanism. *Mar. Geol.* 175, 1–23.
- Terzaghi, K., 1950. Mechanism of landslides. In: Paige, S. (Ed.), *Applications of Geology to Engineering Practice*. Geological Society of America, New York, pp. 83–123.
- Thomas, A.L., 1993. *POLY3D: A Three-Dimensional, Polygonal Element, Displacement Discontinuity Boundary Element Computer Program with Applications to Fractures, Faults, and Cavities in the Earth's Crust*. M.Sc. Unpubl. Thesis, Stanford University, Stanford, CA.
- Varnes, D.J., 1978. Slope movement types and processes. In: Schuster, R.L., Krizek, R.J. (Eds.), *Landslides: Analysis and Control*. National Academy of Sciences, Washington, DC, pp. 11–33.
- Voight, B. (Ed.), 1978. *Rockslides and Avalanches*, 1. Elsevier, Amsterdam.
- Wang, H., 2000. *Theory of Linear Poroelasticity*. Princeton University Press, Princeton, NJ.
- Weertman, J., 1971. Theory of water-filled crevasses in glaciers applied to vertical magma transport beneath oceanic ridges. *J. Geophys. Res.* 76, 1171–1183.
- Westman, R.A., 1965. Asymmetric mixed boundary-value problems of the elastic half-space. *J. Appl. Mech.* 32, 411–417.
- Willemsse, E.J.M., Pollard, D.D., 2000. Normal fault growth: Evolution of tipline shapes and slip distribution. In: Florian, K. (Ed.), *Aspects of Tectonic Faulting*. University of Salzburg, Institute for Geology and Paleontology, Salzburg, pp. 193–226.
- Yamagishi, H., Ito, Y., 1994. Relationship of the landslide distribution to geology in Hokkaido, Japan. *Eng. Geol.* 38, 189–203.